J Mater Sci (2012) 47:1004–1010
DOI 10.1007/s10853-011-5880-2

On measurement of carbon content in retained austenite in a nanostructured bainitic steel

C. Garcia-Mateo · F. G. Caballero · M. K. Miller · J. A. Jimenez

Received: 28 July 2011 / Accepted: 16 August 2011 / Published online: 17 September 2011

Abstract In this study, the carbon content of retained austenite in a nanostructured bainitic steel was measured by atom probe tomography and compared with data derived from the austenite lattice parameter determined by X-ray diffraction. The results provide new evidence about the heterogeneous distribution of carbon in austenite, a fundamental issue controlling ductility in this type of microstructure.

Introduction

New high carbon, high silicon steels have been developed with the purpose of obtaining bainite by transformation at low homologous temperatures ($T/T_m \cong 0.25$, where T_m is the absolute melting temperature). The result is an ultra-fine-scale, carbide-free bainitic microstructure, composed of ferrite plates of $\sim$20–40 nm thickness, and carbon-enriched austenite with two different morphologies. One morphology consists of tens-of-nanometer thick thin films between the plates of bainitic ferrite, and the other type consists of austenite blocks, no larger than a few microns, trapped among the sheaves of bainite [1]. The excellent mechanical properties of these nanostructured steels [2] are intimately related to the resistance of retained austenite to transform during plastic straining [3]. One of the most important factors governing austenite stability is the local carbon enrichment attained after transformation. Thus, the quantification of local carbon concentrations in retained austenite is of fundamental interest both for structure/property studies and for process control.

X-ray diffraction (XRD) measurements of the residual austenite lattice parameter, a_γ, are traditionally used for an overall determination of austenite carbon content. However, a limitation to this technique is that it provides an average value of the carbon content over the volume analyzed and is thus not useful for the local and discrete measurements required for detecting variations of carbon content between films or blocks of austenite.

More localized techniques, such as convergent beam Kikuchi line diffraction patterns (CBKLDP) were used by Zhang and Kelly [4] to determine the lattice parameter, and hence the carbon concentration, in austenite. The advantage of this technique is that the carbon content in regions as small as 10 nm can be determined with sufficient accuracy. However, this technique cannot be applied when the defect density is high in the microstructural feature of interest [5]. In these cases, measurement of the lattice fringe spacing via high-resolution transmission electron microscopy (TEM) was found to be most suitable to determine the austenite lattice parameter in a medium carbon, high silicon bainitic steel transformed at 350 °C [5]. TEM results through several focal series acquired for a number of different regions showed a large variation of the austenite lattice parameter from region to region, proving that carbon in austenite is distributed inhomogeneously in a bainitic microstructure. A similar strong inhomogeneity in the lattice parameters of the retained austenite for a steel similar to that used in this study has been reported by Stone et al. [6] using synchrotron X-ray analysis.

The major disadvantage of the techniques described above is that the local carbon content of austenite is

C. Garcia-Mateo (✉) · F. G. Caballero · J. A. Jimenez
Centro Nacional de Investigaciones Metalúrgicas (CENIM-CSIC), Avda Gregorio Del Amo, 8, 28040 Madrid, Spain
e-mail: cgm@cenim.csic.es

M. K. Miller
Materials Science and Technology Division, Oak Ridge National Laboratory (ORNL), Oak Ridge, TN 37831-6136, USA

determined from the lattice parameter. There is a broad range of opinions in the literature regarding the correlation between lattice parameter and chemical composition of austenite [7–17]. In order to evaluate the different published relationships between the carbon content and the lattice parameter, Scott and Drillet [18] directly measured the carbon content in austenite in TRIP (Transformation Induced Plasticity) steels by electron energy loss spectroscopy (EELS) and compared it with data derived from XRD measurements. From this comparison, it was concluded that there was no 'best' equation defining the relationship between the austenite lattice parameter to the austenite carbon content available in the literature. Nevertheless, within the range of carbon concentration explored (0.2–1.5 wt%), it was possible to exclude some of the existing equations as being unsuitable for application to TRIP steels.

The most recent developments in analytical TEM (STEM (Scanning Transmission Electron Microscope), EELS, and EDS (Energy and Dispersive Spectroscopy)) have enabled atomic-scale chemical analyses. Unfortunately, these approaches have numerous drawbacks, including the reliable interpretation of the results [19], the low accuracy of quantitative analysis of nanoscale features that are smaller than the foil thickness (e.g., features that are embedded in a ferromagnetic matrix), and in particular, when low concentrations of light elements, such as carbon, play a critical role in nanostructure stability.

Precise determination of the carbon content in austenite is one of the biggest challenges in the characterization of this new generation of nanostructured bainitic steels. The technique of atom probe tomography (APT) is very effective for this type of analysis, see for example [20–23]. Whereas atom probe measurements are less indirect, the amount of material analyzed is incredibly small and there is no proof that the data accumulated to date are representative. Diffraction measurements, on the other hand, represent information from a much larger volume of material. In the present study, the carbon contents in austenite were measured by APT and compared with data derived from XRD measurements. This study provides additional [24] and new evidence on the heterogeneous distribution of carbon in austenite, a fundamental issue controlling ductility in this type of microstructure.

Material and experimental procedure

The chemical composition of the steel used in this investigation was Fe-0.98 wt% C-1.46% Si-1.89% Mn-1.26% Cr-0.26% Mo-0.09% V (Fe-4.34 at.% C-2.76% Si-1.82% Mn-1.28% Cr-0.146% Mo-0.09% V). As-received ingots were homogenized at 1200 °C for 48 h in partially evacuated sealed quartz capsules that were flushed with argon. The sealed samples were cooled in air following the homogenization heat treatment, after which, specimens were austenitized for 15 min at 1000 °C and then isothermally transformed at 200 °C for different times before quenching into water. The transformation temperatures, bainite and martensite stat temperatures, B_S and M_S, respectively, were experimentally determined to be 350 and 120 °C, respectively. The microstructure obtained at 200 °C for 240 h (10 days), see Fig. 1, was then tempered at 400 and 450 °C for 30 min.

Quantitative XRD analysis was used to determine the fraction of retained austenite and its lattice parameter. For these experiments, samples were machined, ground and polished with 1 μm diamond paste, and then subjected to several cycles of etching and polishing to obtain an undeformed surface; finally the samples were polished in colloidal silica. X-ray diffraction measurements were performed with a Bruker AXS D8 diffractometer equipped with a Co X-ray tube and Goebel mirror optics to obtain a parallel and monochromatic X-ray beam. A current of 30 mA and a voltage of 40 keV were used. Operational conditions were selected to obtain X-ray diffraction data of sufficiently high quality, e.g., sufficient counting statistics and narrow peak widths. XRD data were collected over a 2θ range of 30–115° with a step width of 0.03° and a counting time of 4 s/step.

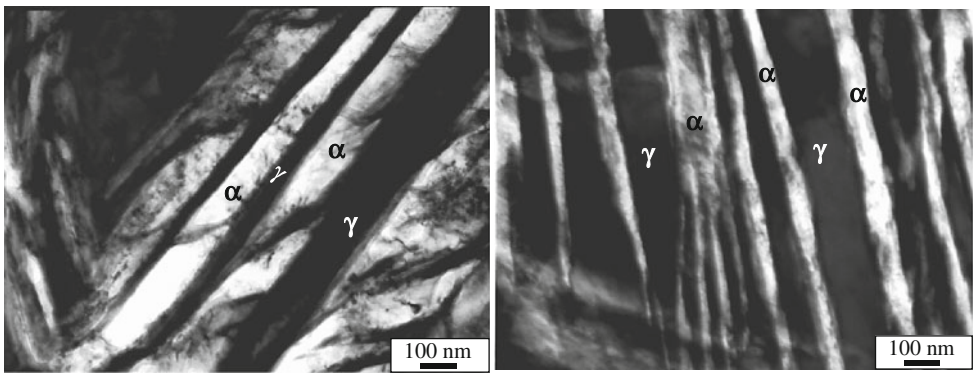

Fig. 1 TEM micrographs of the bainitic microstructure obtained after isothermal transformation at 200 °C for 240 h

The Rietveld method [25] is a powerful tool for calculating the structural parameters from diffraction patterns of polycrystalline bulk materials recorded in a Bragg–Brentano geometry. The application of the Rietveld refinement method to the XRD patterns taken under the experimental conditions used here, instrument functions were empirically parameterised from the profile shape analysis for a corundum standard sample measured under the same conditions. Version 4.0 of Rietveld analysis program TOPAS (Bruker AXS) for the XRD data refinement was used here. The refinement protocol also included the background fitting, zero displacement, the scale factors, the peak breath, the unit cell parameters, and texture parameters. The room temperature structures used in the refinement were ferrite and austenite. The volume fraction of retained austenite and bainitic ferrite was calculated from the integrated intensities of (200) (220), and (311) austenite peaks and the ferrite (002) (112), and (022) planes. Using this number of peaks avoided possible bias due to crystallographic texture [26]. XRD analysis on the homogenized microstructure containing pearlite failed to show any texture [27]. It is also important to note that asymmetry of diffraction peaks may develop due to the presence of internal stresses within the grain of any alloy [28]. Because the current heat treatments were done without any mechanical deformation, the use of symmetric Gaussian peaks is assumed to be valid. For each diffraction pattern, the austenite lattice parameter was determined by applying Cohen's method [11, 29]. The parameters calculated from individual peaks were plotted against $\cos^2\{\theta\}/\sin\{\theta\}$, and the precise lattice parameter, a_γ, were obtained by extrapolating the diffraction angle θ to 90°, with the highest angles being given the greatest weights in the extrapolation. The weighting was performed by regression analysis on a data set containing just one point for the lowest θ value, two identical points for the next θ value, and so on. This is because the largest 2θ are associated with smaller errors in the calculation of lattice parameters. Because of the experimental setup, the amount of specimen surface scanned at large θ is smaller than at lower angles. X-ray experiments were conducted to assess whether this made any difference by making measurements with a rotating specimen to increase the effective area scanned, but this made no significant difference to the measured parameters or volume fractions.

The austenite carbon content was estimated using the well-known Dyson and Holmes' equation that relates the austenite lattice parameter to its composition [10], and it was selected for being the most complete in terms of the influence of different elements in a_γ,. Although this expression has been validated in several publications [30–32], to the effects of substitutional elements it should be taken into account. The bainite transformation in steels is a displacive reaction, in which the ferrite is initially supersaturated with respect to carbon. In the absence of carbide precipitation, prevented in the present steel by the use of silicon, the excess carbon in the bainitic ferrite is subsequently rapidly partitioned into the residual austenite, but substitutional elements do not partition during the bainite reaction [33]; in other words $(x_{Fe}/x_j)_{bulk} = (x_{Fe}/x_j)_\gamma$, where j denotes any substitutional element in the alloy, and x_{Fe} and x_j are the concentrations of Fe and of the substitutional elements, respectively. If this condition is introduced in Dyson and Holmes' equation in conjunction with the fact that $\sum (X_i)_\gamma = 100$, where i denotes all elements in the chemical composition, this gives rise to a system where the austenite carbon content is accurately calculated by an iteration process.

APT specimens were cut from the heat treated material and electropolished by the standard double layer and micropolishing methods [34]. APT analyses were performed in a Cameca Instruments local electrode atom probe (LEAP 2017), which was operated in voltage pulsed mode with a specimen temperature of 60 K, a pulse repetition rate of 200 kHz, and a pulse fraction of 0.2. Examples of three dimensional (3D) carbon atom maps and carbon concentration profiles showing austenite and ferrite regions are reported elsewhere for the same steel [33]. The concentration of carbon was determined from the number of carbon atoms compared with the total number of atoms in small slices perpendicular to one of the axes of a selected volume within austenite regions with a random solid solution. The carbon distribution across interphase interfaces was also determined with the proximity histogram (or proxigram) developed by Hellman et al. [35]. The main advantages of this latter method are that it can accommodate the curvature of nonplanar interfaces and requires significantly less user interaction. Error bars for individual APT values represent the statistical scatter in the concentration profiles due to the number of ions in each slice of the selected volume of analysis. Mean values of a collection of APT measurements are also reported. In this case, their corresponding error bars are standard deviations of the mean value representing the dispersion of the data.

Results and discussion

The volume fraction of the phases present in the microstructure, i.e. bainitic ferrite, retained austenite, and martensite, after isothermal transformation at 200 °C for different times, is listed in Table 1. The presence of martensite in this type of microstructure indicates that the bainite reaction has not yet finished. The microstructure after completion of the bainite reaction (200 °C for 240 h) consists of nano-scale plates of ferrite separated by carbon-enriched

Table 1 Percentage of phases of microstructures after isothermal transformation at 200 °C for different times

Time (h)	Bainitic ferrite	Retained austenite	Martensite
48	34 ± 3	54 ± 3	13 ± 7
96	64 ± 4	26 ± 2	10 ± 6
240	71 ± 2	29 ± 2	–

regions of retained austenite, as shown by TEM examination elsewhere [33]. The volume percentage of the austenite was determined by XRD to be 29 ± 2%. In addition, TEM examination of samples tempered at 400 °C revealed that this higher temperature treatment did not introduce any appreciable change in the microstructure [31, 36], thus extremely fine plates of ferrite and thin films of retained austenite were observed and the austenite volume percentage did not change (29 ± 1%). During tempering at 450 °C, retained austenite decomposes into carbides and ferrite, decreasing its volume fraction from 29 ± 1 to 2 ± 1%, according to XRD. At this temperature, precipitation of ε-carbide in ferrite was also detected [36].

A comparison of the carbon content of retained austenite measured by both XRD and APT is given in Table 2. APT allowed not only the determination of the carbon content within nano-sized retained austenite films, but also an estimation of their size. However, this size might be higher than the estimated value, since the full extent of the coarse features was not observed in the limited volume of analysis, as noted in Table 2.

The XRD values for the carbon content given in Table 2 for samples transformed at 200 °C clearly indicates that as the formation of bainitic ferrite progresses, the austenite is gradually enriched in carbon, from the overall carbon

Table 2 Carbon Content in Austenite obtained by XRD and APT

Heat treatment	XRD, at.%	APT[a], at.%	Thickness of γ measured in APT/nm
200 °C—48 h	4.47 ± 0.44	5.30 ± 2.84	6
200 °C—96 h	5.58 ± 0.44	7.25 ± 3.77	5
200 °C—240 h	6.64 ± 0.44	4.79 ± 3.02	13
		7.39 ± 1.31	30
		5.39 ± 0.18	50[c]
		5.14 ± 3.05	8
		14.4 ± 2.80	5
		6.00 ± 0.20	300[c]
		9.00 ± 0.50	20
		10.21 ± 1.72	18
		11.00 ± 1.78	8
		12.10 ± 1.79	11
		9.01 ± 0.79	20
		4.77 ± 0.24	550[c]
		(8.26 ± 3.20)[b]	
200°C—240 h and tempering at 400 °C for 30 min	6.40 ± 0.44	6.12 ± 0.77	110
		7.32 ± 2.55	50
		9.47 ± 0.41	25
		10.02 ± 0.43	20
		5.74 ± 0.55	250[c]
		11.27 ± 0.79	20
		8.42 ± 0.47	20
		8.40 ± 0.42	60
		7.26 ± 0.65	80
		8.45 ± 0.57	50
		7.27 ± 0.38	32
		(8.16 ± 1.65)	
200°C—240 h and tempering at 450 °C for 30 min	4.23 ± 0.44	3.75 ± 0.95	8
		4.19 ± 1.26	35
		3.72 ± 0.73	15
		(3.89 ± 0.26)	

Also reported the thickness of the austenite regions analyzed by APT

[a] Error bars representing the statistical scatter in the APT composition profiles or proxigrams

[b] Values in bracket are mean values of the APT measurements listed inside the same cell. Their corresponding error bars are standard deviations of the mean value representing the dispersion of a collection of APT measurements

[c] The real thickness might be higher than the represented value since full extent of the coarse feature was not observed in the volume analyzed

content (4.3 at.%) to that given by the incomplete reaction phenomena or T_0'value (7.0 at.%) and well below the para-equilibrium phase boundary value, Ae_3' (20.7 at.%). Before doing a similar analysis of carbon contents measured by APT it is necessary to remember that the film austenite increases at the expense of blocky austenite as transformation progresses [37]. But, it is interesting to note that following Ref. [37], although the proportion of blocky austenite (48%) is much greater than thin films (5%) after 48 h of transformation, APT experiments at this condition correspond to a thin film. Similarly, after 96 h, 16 and 10% of blocks and thin films, respectively are expected. Even in the final microstructure, 240 h, 10 out of 12 measurements, 83%, would fall into the range of thin film morphology, <50 nm. This is related to the fact that coarse features observed in SEM, such as blocky austenite, are not readily observed in randomly located APT samples. Therefore, to some extent, the APT data presented here is biased in terms of the population of the austenite sizes measured. Keeping this in mind, what seems evident is that the amount of C detected in thin films of similar size (5–6 nm) increases as the bainitic ferrite transformation progresses, increasing from 5.3 to 14.4 at.% in Table 2, a result consistent with the progressive C enrichment of austenite as more bainitic ferrite forms and rejects part of the excess of C into it.

Despite the differences between the APT and X-ray analyses, these results are an indirect manifestation of the displacive nature of bainite transformation, such that the original bainitic ferrite retains much of the carbon content of the parent austenite. The partitioning of carbon from bainitic ferrite into the parent residual austenite occurs immediately after the former stops growing. The bainite reaction is expected to cease as soon as the austenite carbon content reaches the value at which displacive transformation becomes thermodynamically impossible, i.e., T_0'value, as the free energies of the residual austenite become less than that of the bainitic ferrite of the same composition.

APT values in Table 2 show strong variations of the carbon concentration between different austenite regions in samples transformed at 200 °C. This result is in agreement with the previously mentioned experiments by APT [20, 23] on carbide-free bainite, by CBKLDP on upper bainite of Zhang and Kelly [4], the fringe spacing measurements on carbide-free bainite by Self et al. [5], and the synchrotron X-ray study by Stone et al. [6] on nanoscale bainitic steels. Similar carbon content ranges were also obtained for the austenite after tempering at 400 °C. However, the loss of carbon in austenite, due to carbide precipitation during tempering at 450 °C, was clearly evident.

Consistent with carbon concentration gradients measured by APT, broad austenite XRD peaks were observed. However, this broadening is also a result of contributions from nano-sized retained austenite particles and local lattice strain. The shape deformation associated with a displacive transformation of austenite in steel can be described as an invariant plane strain with a relatively large shear component. Christian [38] demonstrated that when the shape strain is elastically accommodated, the strain energy scales with the plate aspect ratio (thickness/length), which is why the displacive transformation products in steels, such as Widmanstätten ferrite, bainitic ferrite, and martensite, occur in the form of thin plates. The need to minimize strain energy dictates a thin plate, but this also leads to a minimization of the volume of transformation per plate. Therefore, a plate will tend to adopt the largest aspect ratio consistent with the available free energy change driving the transformation. For ideal circumstances, where the transformation interface remains glissile throughout and where there is no friction opposing the motion of the interface, thermoelastic equilibrium occurs [39]. The aspect ratio of the plate adjusts so that the strain energy is equal to the driving force.

The thermoelastic equilibrium has been widely demonstrated for martensite [39], but it has not been straightforward for bainite. One reason for this is that bainite grows in the form of sheaves, which are a group of connected platelets that grow in parallel formations. The spacing between the platelets is to a large extent controlled by the carbon diffusion field associated with each platelet [40], therefore, the increase in platelet thickness is restricted by the diffusion fields and by the presence of adjacent platelets (i.e., soft and hard impingement effects). A further complication is that the bainite transformation occurs at higher temperatures than those of martensite, where the austenite is mechanically weaker. The shape deformation therefore causes plastic deformation, and the resulting debris from dislocations eventually blocks the transformation interface, which loses coherency. Consequently, platelets of bainitic ferrite are arrested in their growth even when their size is much smaller than the austenite grain size. In this scenario, the plates are expected to become thicker at high temperatures because the yield strength of the austenite will then be lower.

The accommodated strain will not be uniform, decreasing in magnitude in the untransformed austenite as a function of distance from the bainitic ferrite/austenite interface [41], and causing broadening of the diffraction peaks [11]. Scott and Drillet [18] estimated that accommodation strain might provoke a decrease of up to 0.4% in the austenite lattice parameter in 20% of the austenite regions in a TRIP steel. In addition, they compared experimental austenite carbon contents directly obtained by EELS with data derived from XRD measurements of the austenite lattice parameters using expressions available in

the literature relating the carbon content and the lattice parameter for strained and unstrained austenite [12]. Results showed that better overall agreement was obtained with the equation for unstrained austenite than for strained austenite, and equations based on extrapolations from high temperature (unstrained) austenite also gave good results. It was concluded that the lattice parameter of residual austenite in TRIP steels was not greatly affected by local strain.

However, there is another source of broadening in the case of austenite reflections arising from variations of carbon concentrations in the volume sampled by the X-ray beam, a feature inherent to the bainitic transformation. The two essential morphologies of austenite in silicon rich steels, which are transformed to bainite, thin films, and blocks, also contains different quantities of C in solid solution. Thus, during the early stages of transformation, the austenite pattern consisted of narrow peaks associated with a well defined lattice parameter and homogeneous carbon distribution [6]. As transformation progressed, the peak intensity decreased, and together with broad bainitic ferrite peaks, a second set of broad austenite peaks appeared at lower 2θ angles than the initial ones. The latter is caused by the partitioning of carbon from ferrite into retained austenite, thereby leading to an increase in its lattice parameter. The carbon enrichment is greatest in the vicinity of the bainite plates, with distant blocky austenite affected little, thus giving rise to the bimodal austenite parameters [6, 42] for the enriched and non-enriched austenite [31, 43, 44]. This is also the reason why the intensity associated with the larger lattice parameter (carbon-rich) austenite increases in parallel with that of bainitic ferrite. The carbon concentration gradients, and to a lesser extent, the non-uniform strains associated with the plastic accommodation of bainite transformation strain, are responsible for the broad peaks following the commencement of transformation. Some authors have also evoked the formation of isotropic compressive strains due to the partial martensitic transformation of unstable austenite during the final quench to room temperature [17]. As bainitic ferrite develops, the proportion of films of austenite increases, whereas the blocks diminish as they are consumed by the forming ferrite.

In the present study, APT results clearly indicate that in certain austenite regions the measured carbon concentration exceeds the T_0' concentration. This is a consequence of the fact that the austenite films entrapped between neighboring subunits of bainitic ferrite have higher carbon content than the blocks of residual austenite located between the sheaves of bainite [45]. Although such austenite can no longer transform to bainite, it can continue to accumulate carbon from suitable sources. Such circumstances arise naturally during the bainite reaction when a region of austenite, which has been affected by the dumping of carbon from an extant bainite plate, becomes isolated by the formation of new supersaturated bainite plates in close proximity. The subsequent partitioning of carbon from these initially supersaturated bounding plates can raise the carbon content of the entrapped austenite film to any level within the range between the T_0' value (7.0 at.%) and the Ae_3' value (20.7 at.%).

The austenite carbon contents determined by APT are correlated with the thickness of the analyzed austenite regions and compared with the corresponding XRD values in Fig. 2 for the sample transformed at 200 °C for 240 h and after tempering at 400 °C. The diameter of the spheres indicates the thickness in nm of the APT analyzed austenite regions; note that some of the features are bigger than represented, as indicated in Table 2. Nano-scale austenite films with thickness in the range of 5–50 nm show APT carbon content values ranging from 4.79 to 14 at.%, with an average value of 7.41 ± 3.2 at.%, slightly higher than the corresponding XRD and T_0' (7.0 at.%) values and less than the paraequilibrium Ae_3' value (20.7 at.%), lying above the line of unit slope that shows the perfect agreement

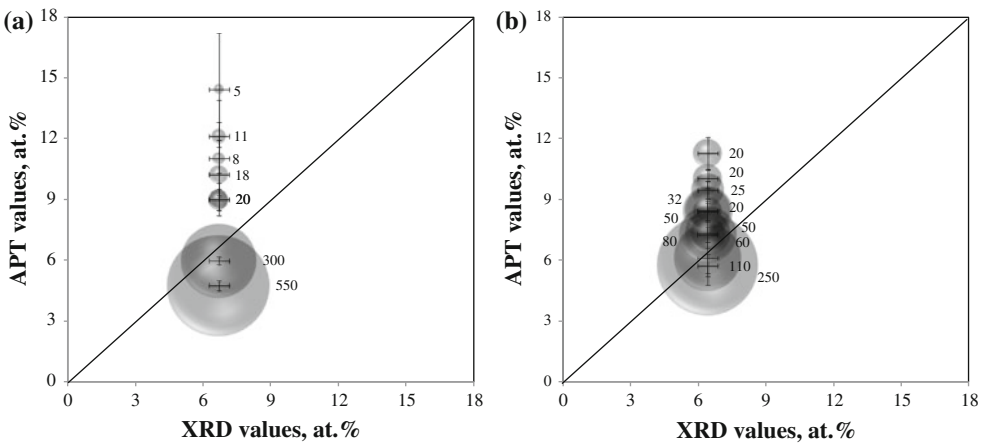

Fig. 2 Carbon content in austenite measured by XRD and APT. The diameter of the spheres indicates the thickness in nm of the APT analyzed austenite regions in **a** sample transformed at 200 °C for 240 h and **b** after tempering at 400 °C. *Points* lying on the line of unit slope show a perfect agreement between XRD and APT values

between XRD and APT values in Fig. 1. Conversely, austenite films with a thickness greater than 50 nm or submicron blocky austenite regions, exhibit APT carbon content ranging from 4.77 to 6 at.%, with an average value of 5.4 ± 0.6 at.%, which is lower than the corresponding XRD and T_0' (7.0 at.%) values, experimental measurements lying on or below the unit slope line in Fig. 1; note that the thickness of those features is higher than the values represented in this graph, since the full extent of the coarse features were not observed in the volume analyzed.

It will be interesting to estimate the APT average austenite content keeping in mind the dependence of the austenite thickness and its carbon content. For this, a simple level rule is proposed; $C_\gamma, = V_{\gamma,\mathrm{f}}\ C_\mathrm{f} + V_{\gamma,\mathrm{b}}\ C_\mathrm{b}$, where the subscripts f and b stand for thin film and block, respectively, and C and V for the carbon content, just reported, and fraction (of the total) of each morphology calculated following Ref. [36]. The result for such calculation is 7.41 at.%, which is in good agreement with the XRD value (see Table 1) and close to the carbon level given by T_0'value and well below the para-equilibrium phase boundary value, Ae_3', as expected from phase transformation theory.

Conclusions

Atom probe tomography has been used to analyze the nanoscale distribution of carbon in retained austenite of low temperature bainitic microstructures, that consists of a mixture of bainitic ferrite plates in a retained austenite matrix. Atom probe microanalysis showed a wide distribution of carbon concentrations in austenite and the results are consistent with previous atom probe data and confirm the X-ray data.

Acknowledgements The authors gratefully acknowledge the support of the Spanish Ministry of Science and Innovation for funding this research under MAT2010-15330. Research at the Oak Ridge National Laboratory SHaRE User Facility was sponsored by the Scientific User Facilities Division, Office of Basic Energy Sciences, US Department of Energy.

References

1. Garcia-Mateo C, Caballero FG, Bhaseshia HKDH (2003) ISIJ Int 43:1238
2. Garcia-Mateo C, Caballero FG (2005) ISIJ Int 45:1736
3. Garcia-Mateo C, Caballero FG (2005) Mater Trans JIM 46:1839
4. Zhang MX, Kelly PM (1998) Mater Charact 40:159
5. Self PG, Bhadeshia HKDH, Stobbs WM (1981) Ultramicroscopy 6:29
6. Stone HJ, Peet MJ, Bhadeshia HKDH, Withers PJ, Babu SS, Specht ED (2008) Proc R Soc Lond Ser A 464:1009
7. Roberts CS (1953) Trans AIME 197:203
8. Ruhl RC, Cohen M (1969) Trans AIME 245:241
9. Ridley N, Stuart H, Zwell L (1969) Trans AIME 245:1834
10. Dyson DJ, Holmes B (1970) J Iron Steel Inst 208:469
11. Cullity BD, Stock SR (2001) Elements of X-ray diffraction, 3rd edn. Prentice Hall, New York
12. Cheng L, Bottger A, de Keijser THH, Mittemeijer EJ (1990) Scr Metall Mater 24:509
13. Onink M, Brackman CM, Tichelaar FD, Mittemeijer EJ, van der Zwaag S (1993) Scr Mater 29:1011
14. Hanzaki AZ, Hodgson PD, Yue S (1995) ISIJ Int 35:324
15. Girault E, Jacques P, Harlet PH, Mols K, van Humbeek J, Aernoudt E, Delannay F (1998) Mater Character 40:111
16. Jacques P, Girault E, Catlin T, Geerlofs N, Kop T, van der Zwaag S, Delannay F (1999) Mater Sci Eng A 273–275:475
17. van Dijk NH, Butt AM, Zhao L, Sietsma J, Offerman SE, Wright JP, van der Zwaag S (2005) Acta Mater 53:5439
18. Scott CP, Drillet J (2007) Scr Mater 56:489
19. Springer Handbook on materials measurement methods (2006). In: Horst Czichos, Tetsuya Saito and Leslie Smith (eds), XXVI edn. Springer, Berlin
20. Bhadeshia HKDH, Waugh AR (1982) Acta Metall 30:775
21. Hall DJ, Bhadeshia HKDH, Stobbs WM (1982) J Phys IV 43:449
22. Stark I, Smith GDW, Bhadeshia HKDH (1990) Metall Trans A 21A:837
23. Peet M, Babu SS, Miller MK, Bhadeshia HKDH (2004) Scr Mater 20:1277
24. Caballero FG, Miller MK, Clarke AJ, Garcia-Mateo C (2010) Scr Mater 63:442
25. Young RA (ed) (1993) The Rietveld Method. University Press, Oxford
26. Dickson MJ (1969) J Appl Crystallogr 2:176
27. Babu SS, Specht ED, David SA, Karapetrova E, Zschack P, Peet M, Bhadeshia HKDH (2005) Metall Mater Trans A 36:3281
28. Acet M, Gehrmann B, Wassermann EF, Bach H, Pepperhoff W (2001) J Magn Magn Mater 232:221
29. King HW, Payzent EA (2001) Can Metall Q 40:385
30. Garcia-Mateo C, Caballero FG, Bhadeshia HKDH (2003) ISIJ Int 43:1821
31. Garcia-Mateo C, Peet M, Caballero FG, Bhadeshia HKDH (2004) Mater Sci Technol 20:814
32. Caballero FG, Garcia-Mateo C, Garcia de Andres C (2005) Mater Trans JIM 46:581
33. Caballero FG, Miller MK, Babu SS, Garcia-Mateo C (2007) Acta Mater 55:381
34. Miller MK (2000) Atom probe tomography. Kluwer Academic/Plenum Press, New York, p 28
35. Hellman OC, Vandenbroucke JA, Rüsing J, Isheim D, Seidman DN (2000) Microsc Microanal 6:437
36. Caballero FG, Garcia-Mateo C, Santofimia MJ, Miller MK, Garcia de Andres C (2009) Acta Mater 57:8
37. Bhadeshia HKDH, Edmonds DV (1983) Metal Sci 17:411
38. Christian JW (1958) Acta Metall 6:377
39. Kurdyumov GV, Khandros LG (1949) Dokl Akad Nauk SSSR 66:211
40. Chang LC, Bhadeshia HKDH (1995) Mater Sci Technol 11:105
41. Cornide J, Miyamoto G, Caballero FG, Furuhara T, Miller MK, Garcia-Mateo C (2011) Solid State Phenom 172–174:111
42. Bhadeshia HKDH, Edmonds DV (1979) Metall Trans 10:895
43. Houillier RL, Begin G, Dube A (1971) Metall Trans 2:2645
44. Matas SJ, Hehemann RF (1961) TMS AIME 221:179
45. Bhadeshia HKDH, Edmonds DV (1980) Acta Metall 28:1265